PNAS RESEARCH ARTICLE | EARTH, ATMOSPHERIC, AND PLANETARY SCIENCES

Millennial-scale variability of the Antarctic ice sheet during the early Miocene

Nicholas B. Sullivan[a,1], Stephen R. Meyers[a], Richard H. Levy[b,c], Robert M. McKay[b], Nicholas R. Golledge[b], and Giuseppe Cortese[c]

Edited by Mathieu Martinez, Universite de Rennes 1, Rennes cedex, France; received March 13, 2023; accepted August 2, 2023 by Editorial Board Member Jean Jouzel

Millennial-scale ice sheet variability (1–15 kyr periods) is well documented in the Quaternary, providing insight into critical atmosphere–ocean–cryosphere interactions that can inform the mechanism and pace of future climate change. Ice sheet variability at similar frequencies is comparatively less known and understood prior to the Quaternary during times, where higher atmospheric pCO_2 and warmer climates prevailed, and continental-scale ice sheets were largely restricted to Antarctica. In this study, we evaluate a high-resolution clast abundance dataset (ice-rafted debris) that captures East Antarctic ice sheet variability in the western Ross Sea during the early Miocene. This dataset is derived from a 100 m-thick mudstone interval in the ANtarctic DRILLing (ANDRILL or AND) core 2A, which preserves a record of precession and eccentricity variability. The sedimentation rates are of appropriate resolution to also characterize the signature of robust, subprecession cyclicity. Strong sub-precession (~10 kyr) cyclicity is observed, with an amplitude modulation in lockstep with eccentricity, indicating a relationship between high-frequency Antarctic ice sheet dynamics and astronomical forcing. Bicoherence analysis indicates that many of the observed millennial-scale cycles (as short as 1.2 kyr) are associated with nonlinear interactions (combination or difference tones) between each other and the Milankovitch cycles. The presence of these cycles during the Miocene reveals the ubiquity of millennial-scale ice sheet variability and sheds light on the interactions between Earth's atmosphere, ocean, and ice in climates warmer than the Quaternary.

paleoclimate | cryosphere | Miocene | cyclostratigraphy

Millennial-scale oscillatory variability in the polar cryosphere (1 to 15 kyr periods) is well characterized in the late Quaternary, where examples include Dansgaard–Oeschger cycles (1), Heinrich Events (2), and Bond Cycles (3), the latter two of which are expressed in North Atlantic ice-rafted debris and document substantial ice-sheet variability. Proposed mechanisms for this variability include the internal mechanics of ice sheets (4, 5), climatic drivers such as shifts in ocean heat transport and changes in atmospheric circulation (6–8), or solar variability (9, 10). While the Northern Hemisphere ice sheets have generally been viewed as a critical amplifier of late Quaternary millennial-scale variability, fundamental questions remain about analogous variability of the Antarctic ice sheet (AIS), especially during the warmer climates of the Neogene, when Northern Hemisphere ice sheets were greatly reduced in extent or absent (11).

This study evaluates early Miocene marine sediments deposited in an ice-proximal Antarctic setting, providing a window into short-term (~1 to 15 kyr) variability of the Southern cryosphere at a time when atmospheric pCO_2 levels were comparable to most scenarios for the coming decades and into the next century (12, 13) (Fig. 1). We investigate an exceptional high-resolution (~500-y sampling interval) clast abundance dataset from AND-2A in the western Ross Sea, reflecting ice-rafted debris and Antarctic ice sheet history on Milankovitch to millennial timescales (14). Although recent work has suggested extensive and dynamic glaciation during the early Miocene, when ice sheets advanced from East and West Antarctica across the Ross Sea continental shelf (15), our study interval represents a time of when ice sheets were predominantly terrestrial and their margins only just extended into marine settings (14). Here, we document strong semi-precession-scale (~10 kyr) cyclicity in clast abundance, in addition to other millennial-scale cycles, and provide the first well-constrained evidence for cyclic AIS volatility on such short timescales during the Miocene.

Geologic Background, Data, and Chronology

The study site AND-2A was drilled as part of the ANtarctic DRILLing (ANDRILL) program in McMurdo Sound to resolve Neogene ice sheet and the tectonic history in a region influenced by West and East Antarctic ice sheets (22, 23). The core was recovered

Significance

Millennial-scale cycles (1–15 kyr periods) are extensively documented in Quaternary climate proxies and linked to complex interhemispheric earth system feedbacks associated with dynamic behavior of large continental-scale ice sheets at both poles. Here, we identify millennial-scale variability in the East Antarctic ice sheet in the early Miocene, a time characterized by warmer climates, higher atmospheric pCO_2, and no large Northern Hemisphere ice sheets. These millennial-scale cycles are modulated by astronomical climate forcing, despite there being no *a priori* reason to expect such patterns to arise from a linear response to Milankovitch Cycles. These patterns likely arise from nonlinear interactions between the atmosphere, ocean, and ice that appear to have characterized Earth's cryosphere for at least the past 20 My.

Author contributions: N.B.S. and S.R.M. designed the research; N.B.S., S.R.M., R.H.L., R.M.M., N.R.G., and G.C. contributed interpretations; N.B.S. and S.R.M. analyzed the data; and N.B.S., S.R.M., R.M.M., N.R.G., and G.C. contributed to the writing of the final manuscript.

The authors declare no competing interest.

This article is a PNAS Direct Submission. M.M. is a guest editor invited by the Editorial Board.

[1]To whom correspondence may be addressed. Email: nbsullivan@wisc.edu.

This article contains supporting information online at https://www.pnas.org/lookup/suppl/doi:10.1073/pnas.2304152120/-/DCSupplemental.

Published September 18, 2023.

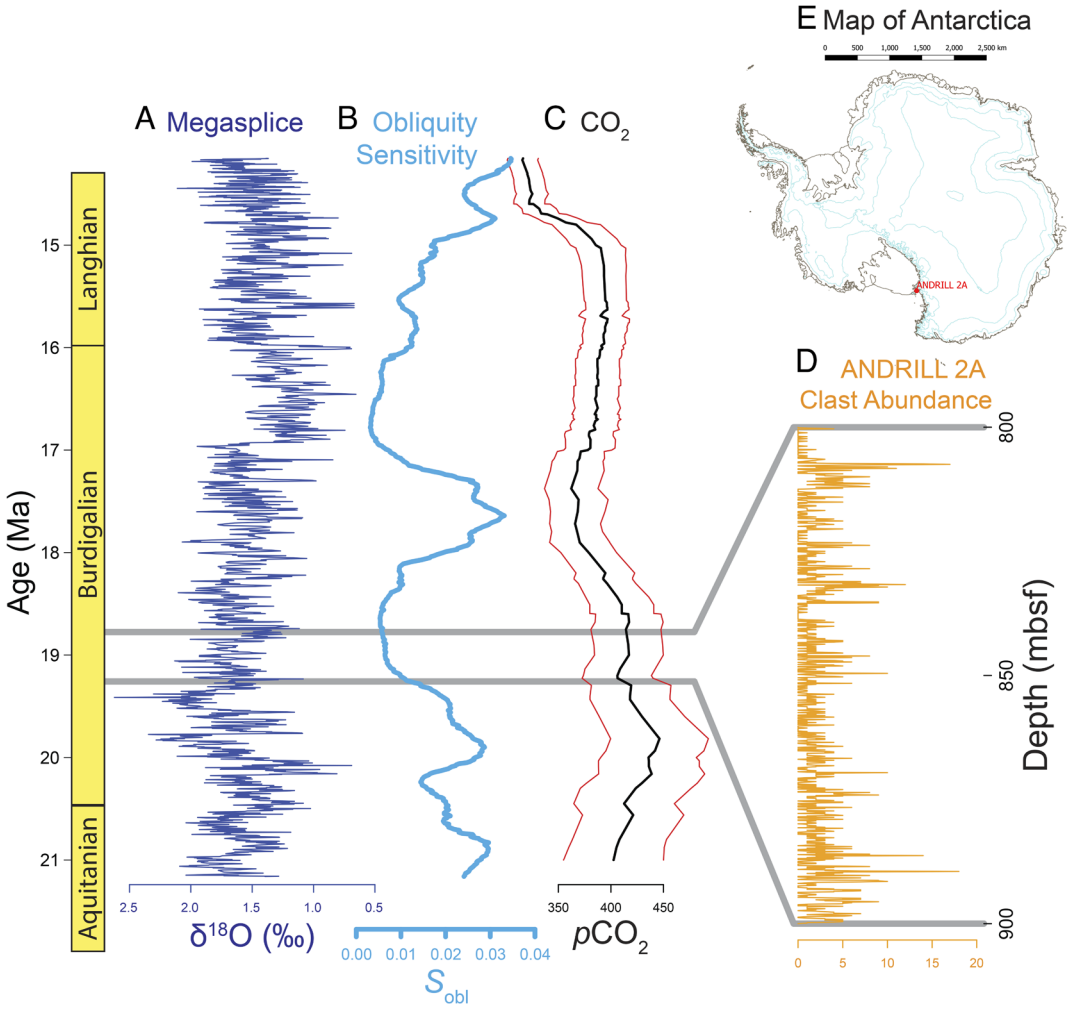

Fig. 1. Temporal context of this study. (*A*) Benthic oxygen isotope megasplice from De Vleeschouwer et al. (16). (*B*) Obliquity sensitivity (S_{obl}) from Levy et al. (17), which is taken as a measure of terrestrial (low S_{obl}) vs. marine-based (high S_{obl}) Antarctic ice sheets. (*C*) Atmospheric pCO_2, showing median (black) and 90% CI (red) of a compilation of proxy data—see Levy et al. (18), and sources therein. (*D*) AND-2A clast abundance data analyzed in this study, which spans ~18.773 to 19.257 Ma (14, 19, 20). (*E*) Map of Antarctica showing the location of AND-2A in McMurdo Sound (21).

from a sea ice drilling platform at the southern end of the Victoria Land Basin at −77.758141, 165.276765 in water 383.57 m deep. A total of 1138.54 m of sediment were cored, with a recovery rate around 98% (24, 25) (*SI Appendix*, Fig. S1). The core section studied here spans the depths 800 to 900 meters below seafloor (mbsf), which is an interval of sandy siltstone with dispersed clasts and sporadic interbedded sands, interpreted to represent relatively continuous deposition (24, 26). Sedimentological data from the core suggest ice-distal conditions with little evidence of grounded ice at the drill site (24, 27, 28). Temperature proxies and geochemical data indicate that cold water temperatures prevailed (−1.3 to 2.6 ± 2.8 °C), and the absence of diatoms implies ice shelf or sea ice cover, or turbid glacial meltwater discharge, both of which can inhibit light penetration (14). Macrofossil remains through the interval include skeletal fragments from serpulid worms, bivalves, bryozoa, and occasional evidence for bioturbation is captured by trace fossils, including *Palaeophycus* and *Chondrites* (26). The long sandy-mudstone sequence stands out in the core and limited evidence for large environmental change suggests climatic variability was relatively small (14).

The clast abundance dataset was generated by manually counting clasts above 2 mm in diameter (gravel) along the cut surface of the archive half sections of the AND-2A core; these counts were subsequently binned into 10-cm depth intervals (14, 19, 29). In glaciomarine strata, increased clast abundance has been linked to fluctuations of the ice sheet margin, due to enhanced ice-rafted debris flux (2, 14). Alternatively, clast abundance can be modulated by glaciomarine mud flux, which can dilute larger clasts and varies in proportion with the distance of the site from the ice sheet grounding lines (30). In either case, previous work has established a direct connection between iceberg-rafted debris and cryosphere behavior (31), and on this basis, we are confident that the clast abundance record here reflects meaningful changes in overall mass balance of the proximal ice sheet.

Age constraints for our study interval are derived from magnetostratigraphy (32, 33) and radioisotopic dates (20), which indicate deposition within chron C6n (18.636 to 19.535 Ma) of the Burdigalian Stage (*SI Appendix*, Fig. S1) (34). The clast abundance data were investigated using *TimeOpt* (35), which generates a floating astrochronology, suggesting an average sedimentation rate of 20.76 cm/kyr, a result that is strong and statistically significant ($P = 0.005$) using an AR1 stochastic null model (*SI Appendix*, Fig. S2). This interpretation is consistent with independent geochronology and suggests an astronomical signal recorded in the clast abundance data that is dominated by precession and eccentricity cycles (Fig. 2 and *SI Appendix*, Figs. S2 and S3). Sub-precession-scale variability has not been previously investigated in

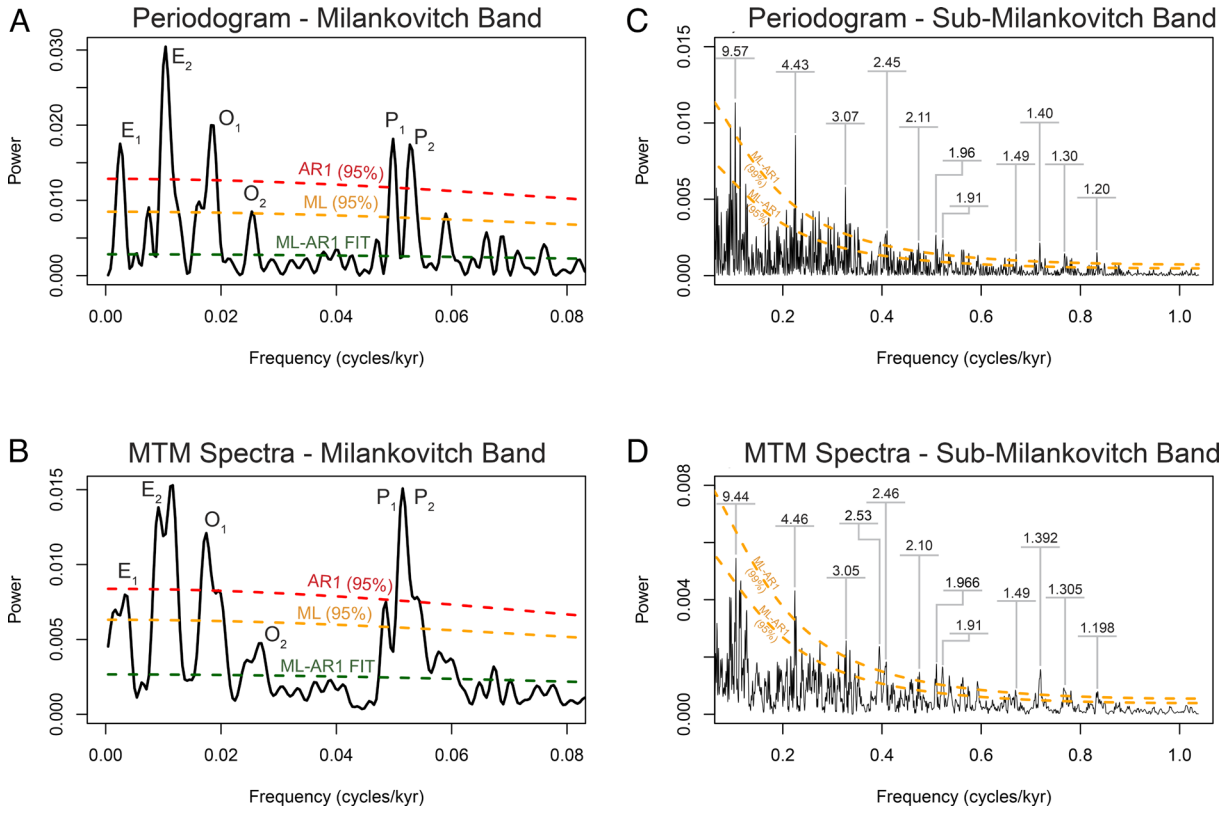

Fig. 2. Power spectral analysis of the ANDRILL 2A clast abundance data from 800 to 900 m, using a TimeOpt-derived timescale. (*A*) Periodogram from 0 to 0.08 cycles/kyr, with a robust AR1 spectral background fit, the robust AR1 95% confidence level, and the conventional AR1 95% confidence level for comparison. Statistically significant eccentricity, obliquity, and precession cycles are identified (E_1 = 401 kyr, E_2 = 96 kyr, O_1 = 55 kyr, O_2 = 39 kyr, P_1 = 20 kyr, P_2 = 19 kyr); note that an astronomical signal has been confirmed in this dataset by TimeOpt analysis (P = 0.005 with multiple testing corrections). (*B*) Same as *A* but using MTM with two 1.5π prolate tapers. (*C*) Periodogram from 0.08 to 1.04 cycles/kyr, with robust AR1 spectral background fit, and robust AR1 95% and 99% confidence levels. Selected high-power millennial-scale peaks are identified that pass the false discovery rate (FDR) test at ≥90% confidence level. (*D*) Same as *C* but using MTM with two 1.5π prolate tapers. A linear trend was removed from the clast abundance data prior to calculation of all power spectra. The spectra are also presented using a log–log scale in *SI Appendix*, Figs. S2 and S3 and select statistically significant power spectra peaks are summarized in *SI Appendix*, Tables S1 and S2, along with their false discovery rate *P*-values.

the clast abundance dataset, but the high temporal resolution (~500-y sampling interval) and the pristine record of astronomically forced ice sheet variability provide a unique opportunity to explore the potential existence of such high-frequency cycles. Observations of mm- and cm-scale bedding in this portion of the core have been attributed to a possible seasonal or tidal influence (26), which is consistent (order of magnitude) with the *TimeOpt*-derived average sedimentation rate of 1 mm = 5 y.

Results

Power spectral analysis of the AND-2A clast abundance data identifies substantial band-limited variance at millennial time scales, and noise model tests indicate numerous spectral peaks that are unlikely to be attributable to stochastic variability (Fig. 2 *C* and *D*). We first consider the significant spectral peaks centering on ~10 kyr, the lowest frequency millennial-scale variability observed in Fig. 2*C*, which also falls within the band of semiprecession (half of a precession cycle). A robust ~10-kyr cycle was observed in the raw clast abundance data (Fig. 2*A*), that cannot be dismissed as an artificial harmonic spectral peak associated with nonsinusoidal variability of precession cycles (36). Complex demodulation of the sub-7 kyr period variability reveals a strong amplitude modulation that is in lockstep with the observed eccentricity and precession signal (Fig. 3*A* and *SI Appendix*, Fig. S4), with spectral energy concentrated at long eccentricity (~400 kyr) and short eccentricity (~100 kyr) periods (Fig. 3*B*), indicating a primary link to astronomical pacing of the East Antarctic ice sheet (EAIS).

An exceptionally narrow and strong spectral peak in clast abundance is identified at a period of 4.4 kyr (0.226 cycles/kyr; multiple test *P*-value = 0.0082), as well as numerous other spectral peaks at periods as short as 1.2 kyr (0.834 cycles/kyr; multiple test *P*-value = 0.0397; *SI Appendix*, Tables S1 and S2). Many of the high-frequency millennial-scale cycles (<7 kyr) observed in Fig. 2 *C* and *D* express strong amplitude modulation coupling to eccentricity and even precession. Moreover, the amplitude modulation of all spectral energy shorter than semiprecession (all variance on timescales <7 kyr, including significant spectral peaks and the intervening spectral "noise" continuum) is characterized by a spectral signature that is remarkably like the Milankovitch signal preserved in the raw clast abundance (*SI Appendix*, Fig. S4).

To further investigate the source of these cycles, we study the bicoherence of the clast abundance data (40) (Fig. 4 and *SI Appendix*, Fig. S5). This analysis is at lower-frequency resolution, as necessitated for bicoherence estimates, but suggests that some of the observed cyclicity is associated with nonlinear interactions between millennial-scale cycles and Milankovitch frequencies. These interactions are summarized in *SI Appendix*, Table S3, but the bicoherence analysis suggests that 8.6, 4.5, 3.7, 3.0, and 1.2-kyr cycles may be partially explained as combination tones arising from the nonlinear interaction with cycles like precession.

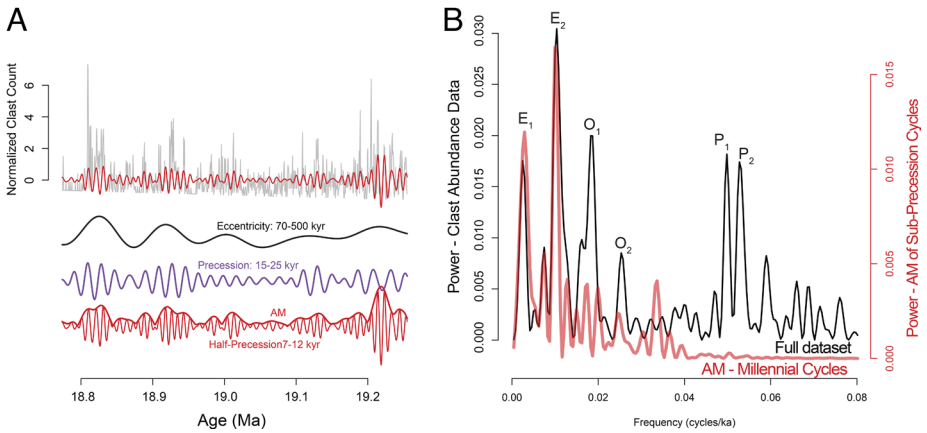

Fig. 3. Milankovitch and millennial-scale cyclic components in the AND-2A clast abundance data, isolated using bandpass filtering (37). The age model is based on an optimal linear sedimentation rate determined by TimeOpt (38) and anchored based on available geochronological constraints to ~18.8 to 19.2 Ma. (*A*) Normalized clast abundance data calibrated by TimeOpt (gray) compared to filtered millennial (<7 kyr periods) cycles (pink), precession cycles (purple), and eccentricity (black). For the millennial cycles, a Hilbert transformation showing amplitude modulation is shown by a thicker red line (39). (*B*) Power spectrum of clast abundance data (black) compared to power spectrum of amplitude modulation of filtered <7 kyr period cycles (red). E_1, E_2, O_1, O_2, P_1, and P_2 indicate the astronomical frequencies as in Fig. 2.

Discussion

The early Miocene forms part of the multi-million-year (multi-Myr) transition from the greenhouse climates of the Eocene to the bipolar icehouse world of the present (41) (Fig. 1). Evidence from benthic $\delta^{18}O$ records suggests that the early Miocene represents a moderately cool time, bounded by a Late Oligocene warming and the mid-Miocene climate optimum (16, 18, 42), with atmospheric pCO_2 levels between 280 and 500 ppm (18, 43, 44). The configuration of continents was broadly similar to the present (45), though the Straits of Panama were open (46), and the Drake Passage became wider and deeper, changing its influence on ocean circulation through the early Miocene (47, 48). Based on these observations, the Miocene is sometimes considered a promising reference for understanding the future behavior of our warming planet (49, 50).

This study has identified strong millennial-scale cyclicity in the East Antarctic ice sheet from 18.773 to 19.257 Ma, via a quantitative evaluation of clast abundance data from the astronomically calibrated 800 to 900-m interval of AND-2A. Multiple testing corrections—which guard against inflated "false positives" that are expected

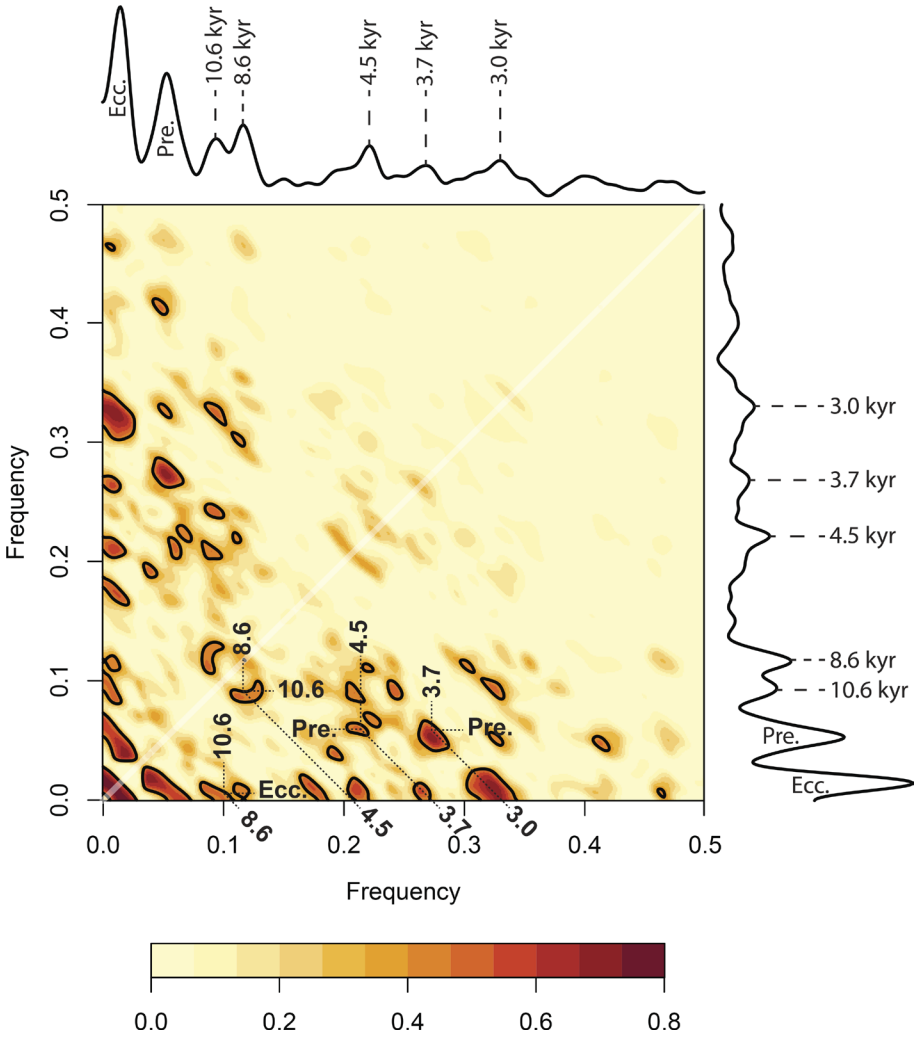

Fig. 4. Bicoherence plot showing nonlinear interactions between cyclic components of the clast abundance data. WOSA power spectra are plotted on the vertical and horizontal axes. Important cyclic components are labeled. Coloration on the chart indicates bicoherence (0 to 1) associated with the given nonlinear interaction, and results that are significant at the 95% confidence level are contoured with a thick black line. Inferred interactions are added as annotations on the chart. The analysis utilizes seven segments with 50% overlap and a Hanning taper. A linear trend was removed from the clast abundance time series prior to analysis. See *SI Appendix*, Fig. S2 for bicoherence results spanning the entire resolvable frequency range (0 to 1.04 cycles/kyr).

when prospecting across broad portions of the power spectrum—indicate numerous statistically significant (FDR $P < 0.10$) cycles. Some of these significant peaks are characterized by adjacent high-power peaks, which are potentially attributable to sedimentation rate variability that manifests as smearing of spectral power. Such sedimentation distortions should more strongly influence high-frequency variability relative to the Milankovitch cycles, due to the nonlinear aspect of the frequency scaling inherent in power spectra. For example, high-power spectral peaks that bracket the statistically significant ~10-kyr cycle (Fig. 2 *C* and *D*) are potentially due to sedimentation rate variability.

Bioturbation is expected to diminish the magnitude of observed millennial-scale cycles more strongly than longer-period Milankovitch cycles. This underscores the value of high accumulation rate settings such as this interval of AND-2A (51), as well as the observed laminations through the study interval, which suggest that mixing by bioturbation is limited. However, some intervals are bioturbated, and given the average sedimentation rate for the clast abundance data (20.76 cm/kyr), and typical sediment mixing depths in the ocean (5 to 10 cm), simulation with a bioturbation mixing model (function "*bioturb*" in Astrochron) indicates that the half-precession cycle in the clast data is likely reduced in magnitude by ~8%, while a 2.5-kyr cycle is reduced by >60%, and cycles near 1 kyr are reduced to <1% of their original size (*SI Appendix*, Fig. S6). Therefore, the true magnitudes of the millennial-scale cycles were likely substantially larger, indicating profound short-term ice sheet variability. This variability may arise from internal mechanisms inherent to ice sheet dynamics (5) or feedbacks between the ocean and atmosphere (6).

The observed amplitude modulation of the ~10 kyr cycles, which closely tracks eccentricity (Fig. 3), indicates that the underlying mechanism has a strong link to Milankovitch forcing (52, 53). Furthermore, the amplitude modulation of all millennial-scale energy shorter than semiprecession (all variance on timescales <7 kyr; *SI Appendix*, Fig. S4) reveals that eccentricity and precession moderate overall millennial-scale variability. Although numerous conceptual models of varying complexity could be envisioned to explain this amplitude modulation, in the simplest interpretation, it reflects changes in proximity of the AND-2A site to the grounding zone or changing ice flux and related rate of iceberg calving. Both processes capture shifts in ice sheet dynamics that diminish or amplify the delivery of clasts associated with millennial-scale variability, whether deriving from cyclic variability or the spectral noise continuum.

Bicoherence analysis (Fig. 4 and *SI Appendix*, Fig. S5) provides evidence that some millennial cycles observed in this dataset arise through nonlinear interaction with others. For example, three cycles we have identified under 5 kyr appear to be combination tones, some of which involve precession, including: 1/4.5 kyr ≈ 1/8.6 kyr + 1/10.6 kyr, 1/3.7 kyr ≈ 1/18.8 kyr + 1/4.5 kyr, and 1/3.0 kyr ≈ 1/18.8 kyr + 1/3.7 kyr (*SI Appendix*, Table S3). By necessity, the bicoherence analysis yields a substantially reduced frequency resolution, which complicates direct comparison to the power spectra in Fig. 2, particularly at the lowest frequencies. For example, an 8.6-kyr cycle is suggested in the bicoherence result, which may represent an interaction between the observed 10.6-kyr cycle and either eccentricity or obliquity (Fig. 4). The Welch Overlapping Spectral Analysis (WOSA) spectrum has insufficient resolution to determine the exact cycle. Assuming the 8.6-kyr cycle is a combination tone, this would imply an interaction between the 10.6-kyr cycle and the primary (~41 kyr) obliquity cycle. However, this is hard to reconcile with the fact that the 41-kyr obliquity cycle is very weak in the raw dataset (Fig. 2). It may instead arise from the influence of an observed 52-kyr cycle.

The observation of a strong half-precession cycle, with eccentricity amplitude modulation, is intriguing. Such cycles are thought to be stronger at low latitudes due to the twice-yearly insolation maxima in the tropics coinciding with the equinox (54, 55). It is possible that low-latitude signals may be transferred to higher latitudes through oceanic or atmospheric pathways (56, 57).

Some of the observed patterns may arise from nonlinear variability within the climate system, atmosphere, or ocean (6, 8). For example, temperature gradients in the atmosphere and ocean exert a strong influence on Southern Hemisphere Westerlies, which influence both the western boundary currents and the position of oceanographic fronts (58, 59). Quasiperiodic fluctuations in these gradients may therefore play some role in the patterns observed here.

To trigger the substantial changes in ice dynamics evident in the sedimentary record, the relatively modest astronomically forced changes in insolation were likely amplified by ice sheet processes. This is supported by evidence from subglacial precipitates that indicate freeze–melt cycles at the Antarctic ice sheet bed are sensitive to millennial-scale climate variability in the late Pleistocene (60). Previous studies have identified four key ice sheet processes that could directly influence cyclicity at these timescales.

The first suggests that dynamic fluctuations arise from basal meltwater and subglacial sediment saturation state (61, 62). In this scenario, linear thickening of an ice stream triggers a nonlinear "switching-on" of basal melting. Once a sufficient thickness of overburden ice has been achieved, it effectively insulates the basal ice and prevents loss of geothermal heat (63–65). Once melted, the basal substrate is weakened, providing reduced resistance to flow and allows ice stream acceleration (5). This acceleration produces enhanced discharge of ice across the grounding line but also thins and lowers the upstream ice. Thinning allows more heat to escape, and the subglacial system freezes again, and discharge is reduced. This system has been shown previously to lead to multicentennial to millennial-scale (2 to 3 kyr) ice dynamic changes across the Antarctic ice sheet (64–66).

A second mechanism relates more directly to the thermal changes taking place within the ice itself. In addition to exogenous heat sources such as geothermal heat flux or atmospheric warming, ice temperatures are governed by endogenous heat production mechanisms such as strain heating (as ice deforms) or heat from sliding friction, as ice slides across a rough bed (65). Both sources of heat soften the ice, and because of a nonlinear temperature/deformation rate relationship, lead to accelerating flow until thinning and conductive heat loss lower ice temperatures, increase ice viscosity, and reduced discharge (67–69). This process has been shown to lag climate forcing by hundreds of years and produce multi-millennial-scale mass loss signatures (70) and in simplified geometry ice sheet simulations to give rise to millennial-scale (>1 kyr) cyclic ice flow oscillations, depending on model parameterization (61). In the latter experiments, it appears that the transition from high-frequency (centennial-scale) to low-frequency (millennial-scale) oscillations arises from a combination of the basal meltwater feedback and local steepening of the ice surface slope, which together extend the zone of temperate ice upstream and also facilitate the down-glacier advection of cold ice (61). This local steepening of the ice surface, and its role in driving accelerated discharge, has also been noted in previous experiments in which increased precipitation under warmer climates drove faster throughput of ice through Antarctic glacier systems and increased discharge to the ocean (71).

Changes in surface mass balance such as this also give rise to the third instance of AIS discharge variability, in which the cooling of the ice sheet surface as its elevation increases leads to more positive mass balance, steepening of the glacier surface, and accelerated flow (72, 73). With accelerated flow and increased ice discharge

at the grounding line (via iceberg calving) comes a lowering of the ice surface, which under warm climates then leads to increased melt or reduced snow accumulation and an overall reduction in mass balance (68, 73, 74). If the net mass balance becomes negative, ice volume will decrease. Simulations exploring the timescale of this mass balance/elevation feedback show that cyclical changes in ice dynamic behavior arise with periods of 1 to 12 kyr, depending on the state of subglacial friction. More rigid beds with lower proportion of deformable sediments (such as would be typical for East Antarctic outlet glaciers, rather than West Antarctic ice streams) give rise to the longer of these periods.

In the fourth mechanism, dynamic changes in ice front position, and the associated changes in ice sheet total mass, arise at multimillennial timescales in places where marine-terminating margins retreat across complex topography (75, 76). In such instances, tipping points in ice sheet volume arise, even in the absence of changes in external climate forcing, on timescales of 5 to 10 kyr, depending on local conditions (76, 77).

The millennial-scale quasiperiodic variations observed in our study interval could arise from any of the four mechanisms outlined above. They could represent oscillatory changes in the atmosphere or ocean system. They could be combination tones arising from nonlinear interactions between other cycles. It is possible, even likely, that the robust millennial cycles observed through our study interval arise from a spectrum of dynamic processes that are continuously interacting with each other and that processes like ice-sheet feedbacks may play a role in amplifying minor changes in external forcing. Our work demonstrates the ubiquity of these signals beyond the Quaternary during times when ice sheets were restricted to the Southern Hemisphere and shows the ways this short-period variability can be influenced by longer Milankovitch Cycles. These findings highlight the sensitivity of the cryosphere to internal and external forcing at a range of timescales, demonstrating the magnitude of change that can arise from minor external forcing.

Conclusions

Significant sub-Milankovitch (1 to 15 kyr) cycles were detected in the 800 to 900 m interval of AND-2A, representing deposition during a warmer-than-present climate from ~18.773 to 19.257 Ma. Cycles at 4.5 kyr, 3.7 kyr, and 3.0 kyr seem to arise from nonlinear interactions (combination tones) of other cycles. An 8.6-kyr cycle could arise from nonlinear interactions as well, although this is less clear and it may be influenced by obliquity or precession. Other millennial-scale variance observed here may be linked to internal feedbacks within the cryosphere that arise from internal dynamics of the ice sheet, rather than the more complex interhemispheric feedbacks that have been associated with Quaternary events at these timescales. Although not primarily the result of Milankovitch forcing, the amplitude and power of these quasiperiodic cycles appear to be strongly influenced and modulated by precession and eccentricity. These findings shed light on the behavior of the early Miocene cryosphere and the ubiquity of millennial-scale variability in large ice sheets.

Materials and Methods

Our analytical approach for investigating potential millennial-scale cyclicity in the AND-2A clast abundance data incorporates four time-series analysis approaches: 1) power spectral analysis with noise model testing, 2) bandpass filtering, 3) complex demodulation, and 4) bicoherence analysis. These methods are selected to provide a comprehensive and statistically rigorous evaluation of millennial-scale variability. All analyses are performed using the Astrochron package (78), developed for the open-source statistical software R (79). An R-script to allow rapid reproduction of the analyses is provided in the *SI Appendix*.

Power spectral analysis allows the quantification of band-limited variance (periodic and quasiperiodic variability), and its evaluation against a stochastic null model. The periodogram is the simplest approach to estimate of spectral power, which also provides the highest-frequency resolution and is thus useful for evaluating the relatively short time series (484 kyr) investigated here. Power spectra are also determined using the Multitaper method (MTM) of Thomson (80), which reduces bias and enhances the statistical stability of the spectral results but at the cost of frequency resolution. The multitaper method calculates a power spectrum by applying several orthogonal "prolate" tapers to the time-series, then averaging the Fourier coefficients following application of a Fourier Transform (80). The suite of prolate tapers used for the MTM spectra is selected to provide an optimal compromise between frequency resolution and bias protection/stability.

Noise model testing is used to evaluate the clast abundance spectra relative to a stochastic null model, to identify potential periodic and quasiperiodic millennial-scale variability. Our evaluation of the statistical significance of potential millennial-scale variability must be conducted with great care, to assure that the significance estimates are meaningful. Prior work has shown that the best noise model to use as a null hypothesis for this dataset is an autoregressive-1 (AR-1) noise model (81), which reflects the behavior of a system that contains both randomness and inertia and provides an appropriate approximation to the spectral background (continuum) for this dataset (*SI Appendix*, Figs. S7 and S8).

Because a strong and statistically significant astronomical signal has been identified in the clast abundance data using the TimeOpt method (35, 78), we can evaluate the power spectra using a robust AR-1 estimation approach that reduces bias on the derived noise model estimates due to the strong astronomical cycles (82, 83). In addition, given that we are prospecting for millennial-scale cycles that are not expected a priori based on a known physics (in contrast to the Milankovitch cycles), it is particularly important to consider multiple-testing corrections, to guard against false positives in our statistical evaluation of hundreds of independent spectral peaks (incorrect rejection of the null hypothesis of stochastic variability). For this purpose, we utilize the FDR approach of Benjamini and Hochberg (84), as previously implemented by Crampton et al.(85) in the R package *astrochron*.

To evaluate potential connections between millennial cycles and astronomical forcing, we assess the amplitude modulation of millennial cycles and compare them to eccentricity and precession cycles observed in the clast abundance data. A Taner bandpass filter (37) is used to isolate frequencies from the eccentricity band, the precession band, and millennial-scale (1 to 15 kyr) band. Complex demodulation of the millennial-scale bandpass output is performed via a Hilbert transform (39), to extract the amplitude modulation (AM), for comparison with eccentricity and precession variability in clast abundance. Power spectral analyses have also been conducted on the resulting AM time-series to quantify observed modulation frequencies.

A final approach used to investigate the source of observed millennial-scale variability is provided by bicoherence, which evaluates potential nonlinear interactions between observed frequencies (40, 53, 86). Bicoherence is a higher-order statistic, which quantifies coupling of individual frequencies (as combination and difference tones). For three frequencies, f_1, f_2, and f_3, high bicoherence indicates that $f_1 + f_2 = f_3$, with the additional property that their phases are also coupled in the data series. We employ the bicoherence approach of Choudhury, Shah and Thornhill (87), which uses WOSA (88), as this method includes improvements to the standard approach that reduce the potential for spurious bicoherence peaks. Note that reliable bicoherence estimates require a substantial increase in bandwidth resolution ("smoothing"), thus bicoherence is reported at a lower-frequency resolution than the power spectral results. We implement this method in the R-package Astrochron (78) and make the new function ("bicoherence") available as a product of the present study. WOSA power spectra are also included for reference to the bicoherence estimates.

Data, Materials, and Software Availability. All study data are included in the article and/or *SI Appendix*. Previously published data were used for this work (29).

ACKNOWLEDGMENTS. This manuscript was greatly improved by the comments of two anonymous reviewers. Bradley D. Singer, Peter M. Sadler, D. Clay Kelly, and John W. Williams provided feedback on an earlier draft of the study. Funding for

this project was provided by the US NSF (NSF-EAR 1151438; S.R.M.) and the Heising-Simons Foundation (HSF 2021-2797; S.R.M.). Additional support was also provided by a Schlanger Fellowship awarded to N.B.S. awarded through the United States Science Support Program. This work was a component of the dissertation of N.B.S., completed in 2022 at the University of Wisconsin–Madison. R.H.L., N.R.G, R.M.M., and G.C. were supported by the New Zealand Ministry of business, Innovation, & Employment through the New Zealand Antarctic Science Platform (Contract ANTA1801).

Author affiliations: [a]Department of Geoscience, University of Wisconsin-Madison, Madison, WI 53706; [b]Antarctic Research Centre, Victoria University of Wellington, Wellington 6012, New Zealand; and [c]Geological and Nuclear Science, Lower Hutt 5040, New Zealand

1. W. Dansgaard, J. W. White, S. J. Johnsen, The abrupt termination of the Younger Dryas climate event. *Nature* **339**, 532–534 (1989).
2. H. Heinrich, Origin and consequences of cyclic ice rafting in the northeast Atlantic Ocean during the past 130,000 years. *Quaternary Res.* **29**, 142–152 (1988).
3. G. C. Bond *et al.*, The North Atlantic's 1–2 kyr climate rhythm: Relation to Heinrich events, Dansgaard/Oeschger cycles and the Little Ice Age. *Geophys. Monogr. Am. Geophys. Union* **112**, 35–58 (1999).
4. P. U. Clark, R. B. Alley, D. Pollard, Northern Hemisphere ice-sheet influences on global climate change. *Science* **286**, 1104–1111 (1999).
5. D. MacAyeal, Binge/purge oscillations of the Laurentide ice sheet as a cause of the North Atlantic's Heinrich events. *Paleoceanography* **8**, 775–784 (1993).
6. R. Alley, P. Clark, L. Keigwin, R. Webb, Making sense of millennial-scale climate change. *Geophys. Monogr. Am. Geophys. Union* **112**, 385–394 (1999).
7. G. Bond *et al.*, A pervasive millennial-scale cycle in North Atlantic Holocene and glacial climates. *Science* **278**, 1257–1266 (1997).
8. S. A. Marcott *et al.*, Ice-shelf collapse from subsurface warming as a trigger for Heinrich events. *Proc. Natl. Acad. Sci. U.S.A.* **108**, 13415–13419 (2011).
9. G. Bond *et al.*, Persistent solar influence on North Atlantic climate during the Holocene. *Science* **294**, 2130–2136 (2001).
10. H. Braun *et al.*, Possible solar origin of the 1,470-year glacial climate cycle demonstrated in acoupled model. *Nature* **438**, 208–211 (2005).
11. C. T. Bolton *et al.*, Millennial-scale climate variability in the subpolar North Atlantic Ocean during the late Pliocene. *Paleoceanography* **25**, PA4218 (2010).
12. IPCC, *Climate Change 2021: The Physical Science Basis. Contribution of Working Group I to the Sixth Assessment Report of the Intergovernmental Panel on Climate Change*, V. Masson-Delmotte *et al.*, Eds. (Cambridge University Press, New York, NY, 2021), p. 3949.
13. M. Meinshausen *et al.*, The RCP greenhouse gas concentrations and their extensions from 1765 to 2300. *Clim. Change* **109**, 213–241 (2011).
14. R. H. Levy *et al.*, Antarctic ice sheet sensitivity to atmospheric CO2 variations in the early to mid-Miocene. *Proc. Natl. Acad. Sci. U.S.A.* **113**, 3453–3458 (2016).
15. J. W. Marschalek *et al.*, A large west Antarctic Ice Sheet explains early Neogene sea-level amplitude. *Nature* **600**, 450–455 (2021).
16. D. De Vleeschouwer, M. Vahlenkamp, M. Crucifix, H. Pälike, Alternating Southern and Northern Hemisphere climate response to astronomical forcing during the past 35 my. *Geology* **45**, 375–378 (2017).
17. R. H. Levy *et al.*, Antarctic ice-sheet sensitivity to obliquity forcing enhanced through ocean connections. *Nat. Geosci.* **12**, 132–137 (2019).
18. R. H. Levy *et al.*, "Antarctic environmental change and ice sheet evolution through the Miocene to Pliocene–a perspective from the Ross Sea and George V to Wilkes Land Coasts" in *Antarctic Climate Evolution*, F. Florindo, M. J. Siegert, L. De Santis, T. R. Naish, Eds. (Elsevier, 2022), pp. 389–521. 10.1016/B978-0-12-819109-5.00014-1.
19. F. M. Talarico, S. Sandroni, Early Miocene basement clasts in ANDRILL AND-2A core and their implications for paleoenvironmental changes in the McMurdo Sound region (western Ross Sea, Antarctica). *Global Planet. Change* **78**, 23–35 (2011).
20. G. Di Vincenzo, L. Bracciali, P. Del Carlo, K. Panter, S. Rocchi, 40 Ar–39 Ar dating of volcanogenic products from the AND-2A core (ANDRILL Southern McMurdo Sound Project, Antarctica): Correlations with the Erebus Volcanic Province and implications for the age model of the core. *Bull. Volcanol.* **72**, 487–505 (2010).
21. K. Matsuoka *et al.*, Quantarctica, an integrated mapping environment for Antarctica, the Southern Ocean, and sub-Antarctic islands. *Environ Model Softw*. **140**, 105015 (2018).
22. G. D. Acton *et al.*, Preliminary integrated chronostratigraphy of the AND-2A core, ANDRILL Southern McMurdo Sound project, Antarctica. *Terra Antarctica* **15**, 211–220 (2008).
23. T. Naish, R. Powell, R. Levy, Background to the McMurdo Ice Shelf Project (Antarctica) Initial Science Volume. (ANDRILL-MIS Science Team, Terra Antartica, 2007), vol. 14, pp. 121–130.
24. C. R. Fielding *et al.*, Sequence stratigraphy of the ANDRILL AND-2A drillcore, Antarctica: A long-term, ice-proximal record of Early to Mid-Miocene climate, sea-level and glacial dynamism. *Palaeogeogr. Palaeoclimatol. Palaeoecol.* **305**, 337–351 (2011).
25. T. Falconer *et al.*, Operations overview for the ANDRILL Southern Ocean McMurdo Sound Project, Antarctica. *Terra Antarctica* **15**, 41–48 (2008).
26. C. R. Fielding *et al.*, "Sedimentology and stratigraphy of the AND-2A core, ANDRILL Southern McMurdo Sound project, Antarctica" in *Studies from the ANDRILL, Southern McMurdo Sound Project, Antarctica*, D. M. Harwood, F. Florindo, F. Talarico, R. H. Levy, Eds. (Terra Antarctica, 2008), pp. 77–112.
27. B. D. Field *et al.*, A sedimentological record of early Miocene ice advance and retreat, AND-2A drill hole, McMurdo Sound, Antarctica. *Geosphere* **14**, 1780–1803 (2018).
28. S. Passchier *et al.*, Early and middle Miocene Antarctic glacial history from the sedimentary facies distribution in the AND-2A drill hole, Ross Sea, Antarctica. *GSA Bull.* **123**, 2352–2365 (2011), 10.1130/b30334.1.
29. K. Panter *et al.*, Petrologic and geochemical composition of the AND-2A core, ANDRILL Southern McMurdo Sound Project, Antarctica. *Terra Antartica* **15**, 147–192 (2009).
30. R. McKay *et al.*, The stratigraphic signature of the late Cenozoic Antarctic Ice Sheets in the Ross Embayment. *GSA Bull.* **121**, 1537–1561 (2009).
31. M. E. Weber, N. R. Golledge, C. J. Fogwill, C. S. Turney, Z. A. Thomas, Decadal-scale onset and termination of Antarctic ice-mass loss during the last deglaciation. *Nat. Commun.* **12**, 1–13 (2021).
32. G. D. Acton, Y. Guyodo, S. A. Brachfeld, "Magnetostratigraphy of sediment drifts on the continental rise of West Antarctica (ODP Leg 178, Sites 1095, 1096, and 1101)" in *Proceedings of the Ocean Drilling Program: Scientific Results* (Texas A & M University, 2002), pp. 1–61.
33. F. Florindo *et al.*, Paleomagnetism and biostratigraphy of sediments from Southern Ocean ODP Site 744 (southern Kerguelen Plateau): Implications for early-to-middle Miocene climate in Antarctica. *Global Planet. Change* **110**, 434–454 (2013).
34. J. Ogg, "Geomagnetic polarity time scale" in *Geologic Time Scale 2020*, F. M. Gradstein, J. G. Ogg, M. Schmitz, G. Ogg, Eds. (Elsevier, 2020), pp. 159–192. 10.1016/B978-0-12-824360-2.00005-X.
35. S. R. Meyers, The evaluation of eccentricity-related amplitude modulation and bundling in paleoclimate data: An inverse approach for astrochronologic testing and time scale optimization. *Paleoceanography* **30**, 1625–1640 (2015).
36. S. R. Meyers, B. B. Sageman, L. A. Hinnov, Integrated quantitative stratigraphy of the Cenomanian-Turonian Bridge Creek Limestone Member using evolutive harmonic analysis and stratigraphic modeling. *J. Sediment. Res.* **71**, 628–644 (2001).
37. Taner M. T., Attributes Revisited (Technical Report, Rock Solid Images, Inc., 1992).
38. S. R. Meyers, Cyclostratigraphy and the problem of astrochronologic testing. *Earth Sci. Rev.* **190**, 190–223 (2019).
39. M. T. Taner, F. Koehler, R. Sheriff, Complex seismic trace analysis. *Geophysics* **44**, 1041–1063 (1979).
40. M. Du, *Comparing Nonlinear Climate Responses to Orbital-insolation During the Early Miocene and Pleistocene: A Bicoherence Study* (University of Wisconsin–Madison, 2013).
41. J. Zachos, M. Pagani, L. Sloan, E. Thomas, K. Billups, Trends, rhythms, and aberrations in global climate 65 Ma to present. *Science* **292**, 686–693 (2001).
42. J. C. Zachos, N. J. Shackleton, J. S. Revenaugh, H. Pälike, B. P. Flower, Climate response to orbital forcing across the Oligocene-Miocene boundary. *Science* **292**, 274–278 (2001).
43. Y. G. Zhang, M. Pagani, Z. Liu, S. M. Bohaty, R. DeConto, A 40-million-year history of atmospheric CO2. *Philos. Trans. Royal Soc. A* **371**, 20130096 (2013).
44. J. W. Rae *et al.*, Atmospheric CO2 over the past 66 million years from marine archives. *Annu. Rev. Earth Planet. Sci.* **49**, 609–641 (2021).
45. C. Scotese, Atlas of Paleogene Paleogeographic Maps (Mollweide Projection), Maps 8–15, Volume 1. The Cenozoic. PALEOMAP Atlas for ArcGIS, PALEOMAP Project, Evanston, IL (2014).
46. A. O'Dea *et al.*, Formation of the Isthmus of Panama. *Sci. Adv.* **2**, e1600883 (2016).
47. Y. Lagabrielle, Y. Goddéris, Y. Donnadieu, J. Malavieille, M. Suarez, The tectonic history of Drake Passage and its possible impacts on global climate. *Earth Planet. Sci. Lett.* **279**, 197–211 (2009).
48. U. Mikolajewicz, E. Maier-Reimer, T. J. Crowley, K.-Y. Kim, Effects of Drake and Panamanian gateways on circulation of an Ocean model. *Paleoceanography* **8**, 409–426 (1993).
49. M. Steinthorsdottir *et al.*, The Miocene: The future of the past. *Paleoceanogr. Paleoclimatol.* **36**, e2020PA004037 (2021).
50. M. Steinthorsdottir, P. E. Jardine, W. C. Rember, Near-future pCO2 during the hot miocene climatic optimum. *Paleoceanogr. Paleoclimatol.* **36**, e2020PA003900 (2021).
51. H. Liu, S. R. Meyers, S. A. Marcott, Unmixing deep-sea paleoclimate records: A study on bioturbation effects through convolution and deconvolution. *Earth Planet. Sci. Lett.* **564**, 116883 (2021).
52. A.-C. Da Silva *et al.*, Millennial-scale climate changes manifest Milankovitch combination tones and Hallstatt solar cycles in the Devonian greenhouse world. *Geology* **47**, 19–22 (2019).
53. T. Hagelberg, N. Pisias, S. Elgar, Linear and nonlinear couplings between orbital forcing and the marine δ18O record during the Late Neocene. *Paleoceanography* **6**, 729–746 (1991).
54. A. Berger, M.-F. Loutre, J. Mélice, Equatorial insolation: From precession harmonics to eccentricity frequencies. *Clim. Past* **2**, 131–136 (2006).
55. D. A. Short, J. G. Mengel, T. J. Crowley, W. T. Hyde, G. R. North, Filtering of Milankovitch cycles by Earth's geography. *Quaternary Res.* **35**, 157–173 (1991).
56. A. Ulfers, C. Zeeden, S. Voigt, M. S. Abadi, T. Wonik, Half-precession signals in Lake Ohrid (Balkan) and their spatio-temporal relations to climate records from the European realm. *Q. Sci. Rev.* **280**, 107413 (2022).
57. Y. Wang *et al.*, Combined high-and low-latitude forcing of East Asian monsoon precipitation variability in the Pliocene warm period. *Sci. Adv.* **6**, eabc2414 (2020).
58. T. E. Whittaker, C. H. Hendy, J. C. Hellstrom, Abrupt millennial-scale changes in intensity of Southern Hemisphere westerly winds during marine isotope stages 2–4. *Geology* **39**, 455–458 (2011).
59. B. L. Hall, G. H. Denton, A. G. Fountain, C. H. Hendy, G. M. Henderson, Antarctic lakes suggest millennial reorganizations of Southern Hemisphere atmospheric and oceanic circulation. *Proc. Natl. Acad. Sci. U.S.A.* **107**, 21355–21359 (2010).
60. G. Piccione *et al.*, Subglacial precipitates record Antarctic ice sheet response to late Pleistocene millennial climate cycles. *Nat. Commun.* **13**, 5428 (2022).
61. W. J. Van Pelt, J. Oerlemans, Numerical simulations of cyclic behaviour in the Parallel Ice Sheet Model (PISM). *J. Glaciol.* **58**, 347–360 (2012).
62. G. K. C. Clarke, S. J. Marshall, C. Veiga-Pires, G. Bilodeau, C. Hillaire-Marcel, "A glaciological perspective on Heinrich events" in *Mechanisms of Global Climate Change at Millennial Time Scales*, P. U. Clark, R. S. Webb, L. D. Keigwin, Eds. (American Geophysical Union, Washington, DC, 1999), pp. 243–262.
63. W. Budd, D. Jenssen, Numerical modelling of glacier systems. *IAHS Publ.* **104**, 257–291 (1975).
64. A. Payne, Limit cycles in the basal thermal regime of ice sheets. *J. Geophys. Res. Solid Earth* **100**, 4249–4263 (1995).
65. F. Pattyn, The variability of the Antarctic ice-sheet response to the climatic signal. *Ann. Glaciol.* **29**, 273–278 (1999).
66. F. Pattyn, Numerical modelling of a fast-flowing outlet glacier: Experiments with different basal conditions. *Ann. Glaciol.* **23**, 237–246 (1996).
67. P. Huybrechts, A 3-D model for the Antarctic ice sheet: A sensitivity study on the glacial-interglacial contrast. *Clim. Dyn.* **5**, 79–92 (1990).
68. P. Huybrechts, Formation and disintegration of the Antarctic ice sheet. *Ann. Glaciol.* **20**, 336–340 (1994).

69. P. Huybrechts, J. Oerlemans, Evolution of the East Antarctic ice sheet: A numerical study of thermo-mechanical response patterns with changing climate. *Ann. Glaciol.* **11**, 52–59 (1988).
70. N. R. Golledge *et al.*, The multi-millennial Antarctic commitment to future sea-level rise. *Nature* **526**, 421–425 (2015).
71. R. Winkelmann, A. Levermann, M. A. Martin, K. Frieler, Increased future ice discharge from Antarctica owing to higher snowfall. *Nature* **492**, 239–242 (2012).
72. R. C. Warner, W. Budd, Modelling the long-term response of the Antarctic ice sheet to global warming. *Ann. Glaciol.* **27**, 161–168 (1998).
73. P. Huybrechts, J. De Wolde, The dynamic response of the Greenland and Antarctic ice sheets to multiple-century climatic warming. *J. Clim.* **12**, 2169–2188 (1999).
74. A. Levermann, R. Winkelmann, A simple equation for the melt elevation feedback of ice sheets. *Cryosphere* **10**, 1799–1807 (2016).
75. W. Budd, P. Keage, N. Blundy, Empirical studies of ice sliding. *J. Glaciol.* **23**, 157–170 (1979).
76. N. Golledge, R. Levy, R. McKay, T. Naish, East Antarctic ice sheet most vulnerable to Weddell Sea warming. *Geophys. Res. Lett.* **44**, 2343–2351 (2017).
77. N. R. Golledge *et al.*, Antarctic climate and ice-sheet configuration during the early Pliocene interglacial at 4.23 Ma. *Clim. Past* **13**, 959–975 (2017).
78. S. R. Meyers, Package 'astrochron'–A Computational Tool for Astrochronology (2014).
79. R Core Team, *R: A Language and Environment for Statistical Computing* (R Foundation for Statistical Computing, Vienna, Austria, 2022).
80. D. J. Thomson, Spectrum estimation and harmonic analysis. *Proc. IEEE* **70**, 1055–1096 (1982).
81. S. R. Meyers, Seeing red in cyclic stratigraphy: Spectral noise estimation for astrochronology. *Paleoceanogr. Paleoclimatol.* **27**, PA3228 (2012).
82. M. E. Mann, J. M. Lees, Robust estimation of background noise and signal detection in climatic time series. *Clim. Change* **33**, 409–445 (1996).
83. M. Patterson *et al.*, Orbital forcing of the East Antarctic ice sheet during the Pliocene and Early Pleistocene. *Nat. Geosci.* **7**, 841 (2014).
84. Y. Benjamini, Y. Hochberg, Controlling the false discovery rate: A practical and powerful approach to multiple testing. *J. R. Stat. Soc. B Methodol.* **57**, 289–300 (1995).
85. J. S. Crampton *et al.*, Pacing of Paleozoic macroevolutionary rates by Milankovitch grand cycles. *Proc. Natl. Acad. Sci. U.S.A.* **115**, 5686–5691 (2018).
86. Y. C. Kim, E. J. Powers, Digital bispectral analysis and its applications to nonlinear wave interactions. *IEEE Trans. Plasma Sci.* **7**, 120–131 (1979).
87. S. M. Choudhury, S. L. Shah, N. F. Thornhill, "Bispectrum and bicoherence" in *Diagnosis of Process Nonlinearities and Valve Stiction* (Springer, 2008), pp. 29–41.
88. P. Welch, The use of fast Fourier transform for the estimation of power spectra: A method based on time averaging over short, modified periodograms. *IEEE Trans. Audio Electroacoustics* **15**, 70–73 (1967).